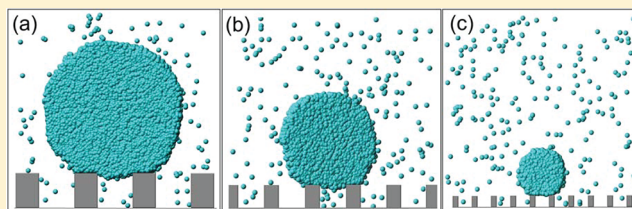


# Wetting on Physically Patterned Solid Surfaces: The Relevance of Molecular Dynamics Simulations to Macroscopic Systems

Azar Shahraz,<sup>†</sup> Ali Borhan,<sup>†</sup> and Kristen A. Fichthorn<sup>\*,‡</sup>

<sup>†</sup>Department of Chemical Engineering and <sup>‡</sup>Department of Physics, The Pennsylvania State University, University Park, Pennsylvania 16802, United States

**ABSTRACT:** We used molecular dynamics (MD) simulations to study the wetting of Lennard-Jones cylindrical droplets on surfaces patterned with grooves. By scaling the surface topography parameters with the droplet size, we find that the preferred wetting modes and contact angles become independent of the droplet size. This result is in agreement with a mathematical model for the droplet free energy at small Bond numbers for which the effects of gravity are negligible. The MD contact angles for various wetting modes are in good agreement with those predicted by the mathematical model. We construct phase diagrams of the dependence of the wetting modes observed in the MD simulations on the topography of the surface. Depending on the topographical parameters characterizing the surface, multiple wetting modes can be observed, as is also seen experimentally. Thus, our studies indicate that MD simulations can yield insight into the large-length-scale behavior of droplets on patterned surfaces.



## INTRODUCTION

Designing surfaces with controllable wettability is important in many practical applications.<sup>1–4</sup> It is now well recognized that the chemical composition and topography of a surface are the two dominant factors that influence wettability, although achieving the elusive combination of these two constituents for a given application is still an area of active research.<sup>5</sup> Regarding the topographical effect, two models have been typically used to describe the configurations of drops on structured surfaces. The first of these is the noncomposite (or the Wenzel model<sup>6</sup>), in which the drop penetrates the surface roughness, in addition to maintaining a contact angle above it. The second model is the composite (or the Cassie–Baxter<sup>7</sup> model) in which the drop resides above the surface asperities with vapor below it. Both of these models can predict contact angles on textured surfaces based on a knowledge of the roughness parameters and the contact angle for a flat surface of the same material. There has been considerable activity associated with assessing these models, and the results are mixed.<sup>8–10</sup> Experimental studies have shown that these models can describe contact angles only for a limited range of surface morphologies.<sup>11,12</sup> Another complicating factor is that droplets exhibit various metastable states, with each corresponding to a local free-energy minimum, thus leading to different wetting modes and contact angles for the same droplet on the same surface. The most stable equilibrium state is not necessarily attained, as a result of the free-energy barrier between the metastable and stable modes.<sup>13–22</sup> In the interest of designing surfaces with controlled wettability, it is clearly desirable to develop robust models that can describe history-dependent droplet configurations on surfaces with a variety of different topographies.

Molecular dynamics (MD) simulations can be used to describe many aspects of droplet wetting on structured surfaces. For example, several MD studies have probed the influence of surface patterning on droplet wetting modes and contact angles.<sup>23–30</sup> MD simulations have also been used to quantify the kinetics of droplet-wetting transitions between the Cassie and Wenzel modes.<sup>31–35</sup> Recent studies have demonstrated that MD simulations can describe contact-angle hysteresis.<sup>36–38</sup> A clear strength of these simulations is that they do not rely on continuum assumptions, they are able to resolve the influence of atomic-scale phenomena on wetting, and, provided that sufficiently large systems can be probed, they can resolve the interplay of molecular and continuum phenomena. For example, the studies of Weijs et al. and Ritos et al. demonstrate that nanoscale phenomena can play an important role in bubbles<sup>39</sup> on superhydrophobic surfaces and in advancing and receding contact angles of nanoscale droplets on solid surfaces.<sup>40</sup> However, a concern has been the limited range of length and time scales that can be covered in a typical MD simulation because these do not extend far beyond the nanoscale and they fall short of the length and time scales relevant to experimental studies. Recent studies have demonstrated that the time limitation can be overcome in special simulations that focus on the kinetics of wetting transitions.<sup>31–35</sup> The recent work of Giacomello et al.<sup>35</sup> indicates that their continuum model can describe many aspects of the Cassie-to-Wenzel transition, although a precise continuum description of the free-energy barrier remains elusive. Despite this progress, many aspects of the relationship

Received: June 21, 2013

Revised: August 14, 2013

Published: August 16, 2013

between nanoscale MD simulations and macroscale experiments remain unresolved.

In this Article, we address the relevance of nanoscale MD simulations to the wetting of liquid droplets on macroscopic patterned surfaces in experimental systems. We demonstrate that the wetting modes and contact angles of droplets on grooved solid surfaces are independent of the droplet size if the dimensions of the pattern are scaled by the droplet radius. Our results are consistent with a macroscopic model<sup>29</sup> for the free energies of various droplet wetting modes in the limit of a negligible gravitational effect. Contact angles resulting from our MD simulations are also in excellent agreement with those predicted by the macroscopic model. Furthermore, MD simulations exhibit metastable wetting states, similar to those in experiments. Thus, our studies indicate that MD simulations can provide considerable insight into macroscopic experimental studies of droplet wetting.

## SIMULATION METHODS

We consider the wetting of a periodically grooved solid surface by an infinitely long (periodic) cylindrical Lennard-Jones (LJ) liquid droplet. The grooves are characterized by width  $G$  and height  $H$  and are separated by steps of width  $W$ , as shown in Figure 1. The surface is periodic in the  $y$  direction and infinite

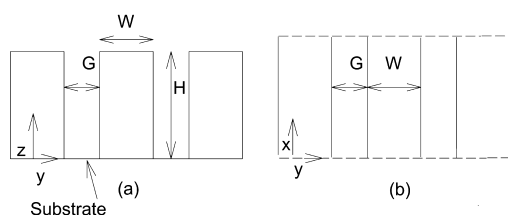


**Figure 1.** Side view (a) and top-down view (b) of the periodically grooved surface characterized by groove width,  $G$ , groove height,  $H$ , and step width,  $W$ .

in the  $x$  direction (Figure 1). The cylindrical droplet is infinite along its long axis (the  $x$  axis in Figure 1), which allows us to

use periodic boundary conditions to simulate a larger droplet for a fixed number of atoms.<sup>41</sup> Moreover, because the curvature of the contact line of a cylindrical droplet is zero, the contact angle of a cylindrical droplet is not affected by the line tension.<sup>42</sup> The number of atoms used to simulate the droplets ranged from 3196 to 28 550.

To describe pairwise interactions between fluid (f) atoms  $i$  and  $j$  separated by a distance of  $r_{ij}$ , we use a truncated LJ potential given by

$$u_{ff}(r_{ij}) = \begin{cases} 4\epsilon_{ff} \left[ \left( \frac{\sigma_{ff}}{r_{ij}} \right)^{12} - \left( \frac{\sigma_{ff}}{r_{ij}} \right)^6 \right] & \text{if } r_{ij} \leq r_c \\ 0 & \text{otherwise} \end{cases} \quad (1)$$

where  $r_c = 3.8\sigma_{ff}$  is the cutoff distance,  $\sigma_{ff}$  is the length parameter, and  $\epsilon_{ff}$  is the energy parameter. The energy parameter is fixed at a value of  $\epsilon_{ff}/k_B = 120$  K, where  $k_B$  is the Boltzmann constant and  $\sigma_{ff}$  and  $\epsilon_{ff}$  are used as the length and energy scales, respectively, to make the equations dimensionless. We also use an LJ potential to describe the interaction of fluid-phase atoms with the solid surface (s). For patterned surfaces, the sum of pairwise LJ interactions can be coarse-grained to enhance the computational efficiency. Here, we use our recently developed patterned-surface potential<sup>45</sup> to describe fluid–solid interactions. The parameters for this potential are set to  $\sigma_{fs} = 0.921\sigma_{ff}$ ,  $\sigma_{ss} = 1.2\sigma_{fs}/2^{1/2}$ , and  $\rho_s = 2^{1/2}/\sigma_{ss}^3$ , with the value of  $\epsilon_{fs}$  selected so as to achieve the desired equilibrium contact angle for the droplet on a flat substrate, as described below.

To simulate the fluid-phase atoms, we used MD in the canonical ensemble, with a constant number, volume, and temperature. We integrated the equations of motion using a fourth-order predictor-corrector algorithm with a time step of 4 fs, and we used the Nosé-Hoover thermostat<sup>43,44</sup> to maintain a temperature of  $T = 0.7\epsilon_{ff}/k_B$ . To generate a cylindrical droplet of radius  $R$ , we placed  $16R^2$  atoms at fcc lattice sites on half of an  $8 \times 2R \times 2R$  rectangular prism and allowed the system to

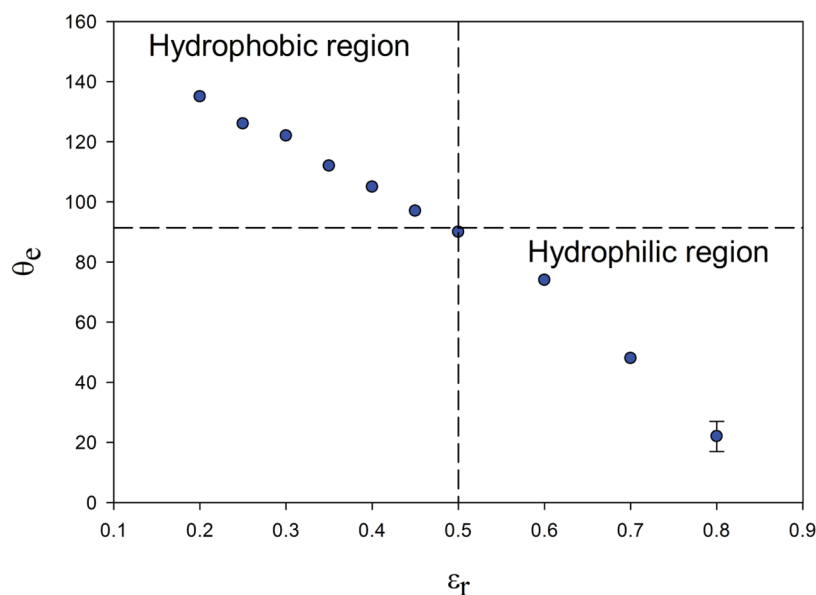


**Figure 2.** Equilibrium contact angle on a flat surface  $\theta_e$  as a function of the relative energy parameter  $\epsilon_r$ . The error bar represents the uncertainty in the computed contact angles. The surface is designated as hydrophobic for  $\theta_e \geq 90^\circ$  and hydrophilic for  $\theta_e < 90^\circ$ .

equilibrate at a temperature of  $T = 2\epsilon_{\text{ff}}/k_B$  for about 1 ns. Then the system was cooled to  $T = 0.7\epsilon_{\text{ff}}/k_B$  in a rectangular prism with dimensions of  $8 \times 7R \times 7R$  to form a condensed cylindrical droplet. For a Cassie initial configuration, the resulting droplet was cut into halves and the upper half was placed over the solid surface such that the center of mass of the drop was centered over a groove, with the lower-most atom initially a distance of  $0.8\sigma_{\text{ff}}$  above the steps to avoid strong repulsion from the solid surface. To achieve an epitaxial Cassie initial configuration, the center of mass of the droplet was centered over a step. For simulations with a Wenzel initial configuration, the solid–liquid interaction energy was initially increased to allow the liquid to fill the grooves and subsequently reduced to its intended value for the simulation.

MD simulations with different initial droplet configurations were performed for different surface geometries, and the apparent contact angle  $\theta$  was monitored as a function of time. Because the observed drop profiles had constant curvature, we determined the contact angle by measuring the apex height and basal length of the best-fit circular interface for the droplet profile.<sup>24</sup> The interface position was determined by calculating the local density of the fluid and recognizing that the maximum variation in local density occurs at the interface.<sup>46</sup> The system was considered to be equilibrated when the contact angle as a function of time reached a plateau value. The total simulation time for achieving equilibrium was 5–15 ns, depending on the system size.

The affinity of the liquid for the solid surface was varied by changing the relative liquid–solid interaction energy  $\epsilon_r$ , which is defined as  $\epsilon_r = \epsilon_s/\epsilon_{\text{ff}}$ . For different relative liquid–solid interaction energies, the corresponding contact angle  $\theta_c$  on a smooth substrate was used to characterize the surface as either hydrophobic or hydrophilic. For sufficiently small  $\epsilon_r$ , the surface is hydrophobic, with  $\theta_c \geq 90^\circ$ , as shown in Figure 2. Figure 2 indicates that the surface is hydrophobic when  $\epsilon_r < 0.5$  and hydrophilic when  $\epsilon_r \geq 0.5$ . For all of the simulations in this study, we used  $\epsilon_r = 0.25$ , corresponding to an equilibrium contact angle of  $\theta_c = 126 \pm 5^\circ$  on a smooth substrate. As we will discuss below, a thermodynamic analysis of our system<sup>29</sup> indicates that the equilibrium contact angle is the key variable that expresses the identities of the liquid and solid-substrate material when the effects of gravity are negligible.

## RESULTS AND DISCUSSION

Figure 3 shows the different wetting modes observed in this study. These include the Cassie, Wenzel, and epitaxial Cassie

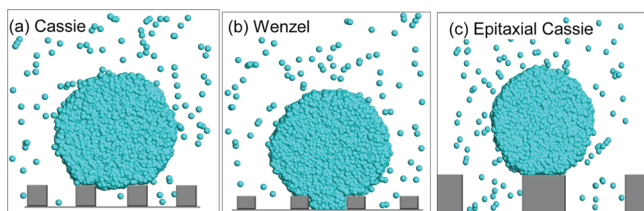


**Figure 3.** Various wetting modes observed in this study.

modes. The epitaxial Cassie mode, in which the droplet resides completely on top of a single step, becomes the energetically favored wetting mode when the dimensions of the groove pattern approach the size of the droplet (i.e., for sufficiently high and wide steps separated by wide grooves). This wetting configuration has been observed experimentally.<sup>47,48</sup>

In a previous study,<sup>29</sup> we presented a model to describe the free energies of droplets in each of the wetting modes in Figure 3. In general, the free-energy difference per unit length  $\Delta E$  between a system consisting of a droplet on the patterned surface and a surface without a droplet is given by

$$\Delta E = A_{lv}\sigma_{lv} + A_{sl}(\sigma_{sl} - \sigma_{sv}) + F_g \quad (2)$$

where  $A_{lv}$  is the area per axial length of the liquid–vapor interface,  $A_{sl}$  is the area per axial length of the solid–liquid interface, and  $\sigma_{lv}$ ,  $\sigma_{sl}$ , and  $\sigma_{sv}$  are the liquid–vapor, solid–liquid, and solid–vapor interfacial energies, respectively. The first two terms on the right-hand side of eq 2 represent interfacial energies, and the last term,  $F_g$ , reflects the effect of gravity. The expressions for  $A_{lv}$ ,  $A_{sl}$ , and  $F_g$  depend on the wetting mode.

Equation 2 can be written in dimensionless form with  $\overline{\Delta E} = \Delta E/\sigma_{lv}R_0$ , where  $R_0$  is the cylindrical-equivalent droplet radius, and with  $A_{lv}$  and  $A_{sl}$  expressed in terms of the dimensionless parameters  $\bar{H} = H/R_0$ ,  $\bar{W} = W/R_0$ , and  $\bar{G} = G/R_0$  characterizing the surface topography, as well as the contact angle  $\theta$ . For example, in the Cassie mode, we have

$$\overline{\Delta E}_C = 2 \left[ \frac{\pi(\theta - \cos \theta_c \sin \theta)^2}{\theta - \sin \theta \cos \theta} \right]^{1/2} + n\bar{G}(1 + \cos \theta_c) + Bo \left[ \frac{2}{3} \left( \frac{\pi \sin^2 \theta}{\theta - \sin \theta \cos \theta} \right)^{3/2} + \pi \left( \bar{H} - \left( \frac{\pi \cos^2 \theta}{\theta - \sin \theta \cos \theta} \right)^{1/2} \right) \right] \quad (3)$$

where  $n$  is the number of grooves underneath the droplet and the Bond number,  $Bo = \rho g R_0^2 / \sigma_{lv}$ , depends on the density  $\rho$  of the liquid and the gravitational acceleration  $g$ . In the limit  $Bo \rightarrow 0$ , the effect of gravity is negligible, and the dimensionless free energy per unit length becomes independent of drop size in eq 3. The same is true for the other wetting modes in Figure 3.<sup>29</sup> This implies, for example, that a water droplet with a radius of  $R_0 = 0.1$  mm on a surface with  $G = W = H = 0.01$  mm will have the same minimum-energy wetting configuration (wetting mode and contact angle) as that for a water droplet with a radius of 10 nm on a surface with  $G = W = H = 1$  nm because  $\bar{H}$ ,  $\bar{W}$ , and  $\bar{G}$  are the same on both surfaces and the Bond number is small for both droplets. Indeed, this implies that a nanoscale MD simulation can predict macroscale wetting configurations as long as the droplet is sufficiently large that its interfacial energies exhibit continuum-like behavior.

To test the ramifications of this prediction, we ran a series of MD simulations. In the first set of simulations, we studied droplets of different sizes on surfaces with the same scaled surface topography. The droplet radii from MD are  $R_0 = (12 \pm 2)\sigma_{\text{ff}}$ ,  $(25 \pm 2)\sigma_{\text{ff}}$ , and  $(50 \pm 2)\sigma_{\text{ff}}$  corresponding to 3196, 12 433, and 28 550 atoms, respectively, and the surface topography is characterized by  $\bar{H} = 0.45 \pm 0.03$ ,  $\bar{G} = 0.45 \pm 0.03$ , and  $\bar{W} = 0.32 \pm 0.02$ . The results are shown in Figure 4 and demonstrate that the droplet is in the Cassie mode in all three cases. The contact angles of the droplets in Figure 4a–c are  $140 \pm 5^\circ$ ,  $141 \pm 5^\circ$ , and  $142 \pm 5^\circ$ , respectively. Using  $n = 1$  and  $\theta_c = 126^\circ$  (the same values as in the MD simulations) in eq 3 for the same scaled surface parameters, the corresponding model prediction for the contact angle in all three cases is  $\theta = 139^\circ$ , which agrees well with the MD results.

In addition to exhibiting a droplet-size invariance of the wetting mode and contact angle for a fixed scaled surface topography, the MD simulations also show the same wetting-mode transitions as the model.<sup>29</sup> We performed a series of



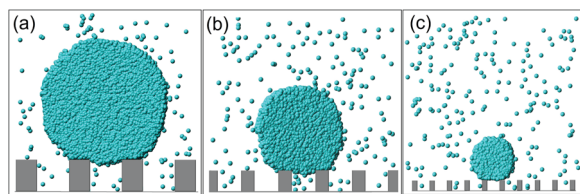


**Figure 4.** Effect of droplet size on wetting mode and apparent contact angle for surfaces with the same scaled topography ( $\bar{G} = \bar{H} = 0.45 \pm 0.03$  and  $\bar{W} = 0.32 \pm 0.02$ ): (a)  $R_0 = (50 \pm 2)\sigma_{ff}$  (b)  $R_0 = (25 \pm 2)\sigma_{ff}$  and (c)  $R_0 = (12 \pm 2)\sigma_{ff}$

simulations in which  $\bar{G}$ ,  $\bar{H}$ , and  $\bar{W}$  were varied, and we recorded the wetting mode and contact angle for each configuration. The results are shown in Figures 5–7, where the effect of groove

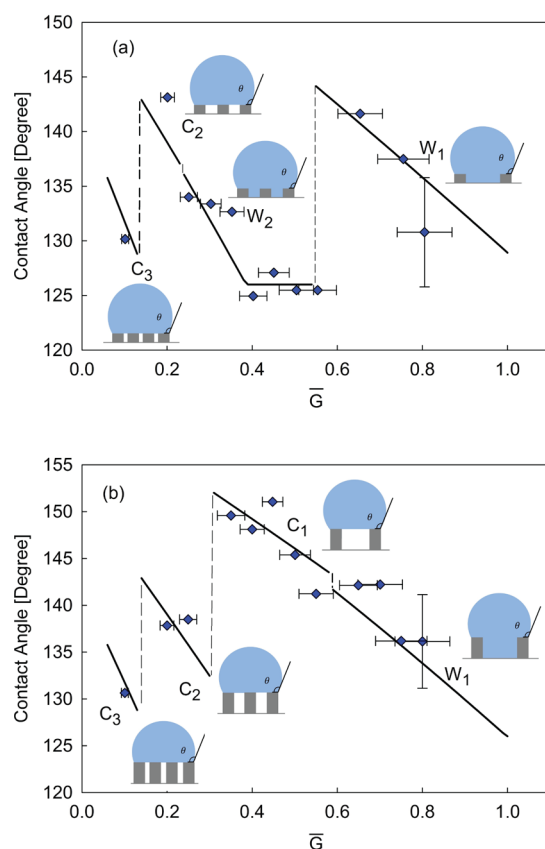


**Figure 5.** Effect of groove width  $\bar{G}$  on the apparent contact angle for a step width of  $\bar{W} = 0.32 \pm 0.03$  and step heights of (a)  $\bar{H} = 0.10 \pm 0.01$  and (b)  $\bar{H} = 0.40 \pm 0.03$ . The solid lines represent predictions of the mathematical model in ref., and the symbols correspond to MD simulations. The vertical error bar depicts the representative uncertainty in the MD contact angles, and the horizontal error bars indicate the uncertainty in the MD value of  $R_0$ .

width, step width, and step height on the contact angle are compared to those predicted by the model for the same wetting configuration. Each equilibrium wetting configuration in Figures 5–7 is identified by a letter indicating the wetting mode, followed by a number denoting the number of grooves spanned by the droplet. For example,  $W_1$  represents the Wenzel state with one liquid-filled groove beneath the droplet.

The effect of the groove width on the contact angle and wetting mode is shown in Figure 5 for two different values of the step height ( $\bar{H} = 0.1 \pm 0.01$  and  $0.4 \pm 0.03$ ) with a fixed

step width of  $\bar{W} = 0.32 \pm 0.03$ . There is excellent agreement between the wetting modes and contact angles predicted by the macroscopic model and those obtained from MD simulations for the corresponding lowest-energy wetting modes. Figure 5 also shows the role of surface roughness in producing discontinuities in the apparent contact angle as the surface topography or drop size changes. For the widest gap in Figure 5a, the droplet remains in the  $W_1$  configuration as its contact angle increases with decreasing gap width—the contact line is pinned at the step edges—until it transitions to the  $W_2$  mode at  $\bar{G} = 0.55 \pm 0.04$ , where the contact line is unpinned and the contact angle is abruptly reduced to  $\theta = \theta_e$ . As  $\bar{G}$  is further reduced, the contact line remains unpinned and moves toward the outer step edges with a nearly constant apparent contact angle until it becomes pinned again at  $\bar{G} = 0.39 \pm 0.03$  and the contact angle begins to increase in the  $W_2$  mode. A small jump in the contact angle is observed in the transition from  $W_2$  to  $C_2$  as the liquid that resided within the gap in the Wenzel mode is pushed above the surface roughness in the Cassie mode. The contact line remains pinned in the  $C_2$  mode as the gap is further reduced until it becomes energetically favorable for the drop to jump across a third groove to enter the  $C_3$  mode. We note that the contact line remains pinned in the jump from  $C_2$  to  $C_3$  (as opposed to the jump from  $W_1$  to  $W_2$ ). For higher steps, as shown in Figure 5b, we observe a sequence of such pinned wetting-mode transitions. In comparing Figure 5b to Figure 5a, we note that the  $W_2$  wetting mode becomes energetically unfavorable for higher steps.

Figure 6 illustrates how the apparent contact angle and wetting mode of the droplet are affected by the step width  $\bar{W}$  for two different values of the groove width ( $\bar{G} = 0.16 \pm 0.01$  and  $0.64 \pm 0.05$ ) with a fixed step height of  $\bar{H} = 0.64 \pm 0.05$ . For the widest step in Figure 6a, the droplet is in the  $C_1$  state, with an unpinned contact line and  $\theta = \theta_e$ . As the step width is reduced, the contact line becomes pinned to the step edges and the contact angle increases. After a transition to the unpinned  $C_2$  state, reducing the step width causes the droplet to go through a series of wetting-mode transitions in which the contact line remains completely pinned. For the wider groove in Figure 6b, the droplet begins in the pinned epitaxial Cassie (EC) state, and the contact line remains pinned as the droplet undergoes a series of wetting-mode transitions with decreasing step width.

Figure 7 shows the dependence of the contact angle and wetting mode on the step height  $\bar{H}$  for two groove widths ( $\bar{G} = 0.16 \pm 0.01$  and  $0.45 \pm 0.04$ ) with a fixed step width of  $\bar{W} = 0.32 \pm 0.03$ . The contact angle and wetting mode are essentially independent of the step height for the smaller gap (Figure 7a)]. For the larger gap in Figure 7b, there is a wetting-mode change from  $W_1$  to  $C_1$  as the step height increases. However, within the uncertainty in determining apparent contact angles from the MD simulations, the contact angle remains nearly the same. This is consistent with our macroscopic model<sup>29</sup> as well as with previous MD simulations<sup>28</sup> and experiments.<sup>49</sup>

In a previous study,<sup>29</sup> we compared the predictions of our model to experimental data<sup>50</sup> for anisotropic droplet wetting on grooved solid surfaces. We showed that for small and finite Bond numbers the contact angles predicted by our model are in good agreement with the contact angles measured from optical images of the droplet taken parallel to the surface grooves.<sup>29</sup> Also, we find excellent agreement between the wetting modes and contact angles predicted by MD simulations and our macroscopic model over a wide range of surface features and

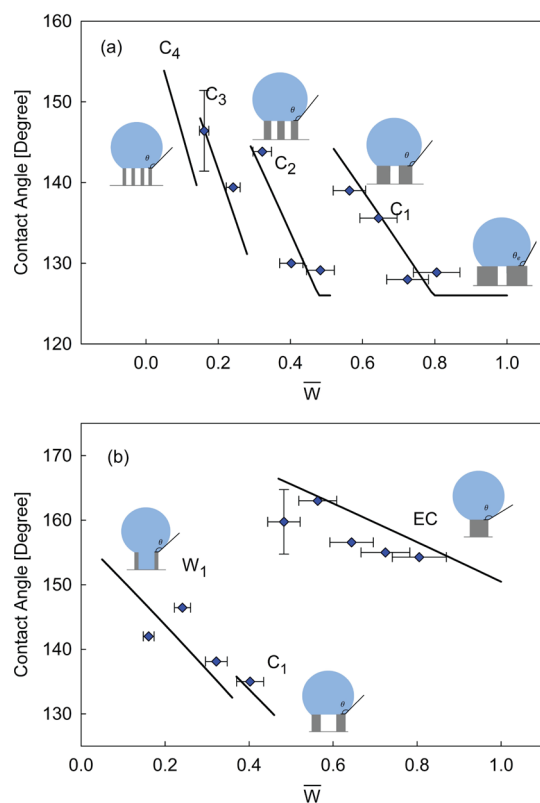


**Figure 6.** Effect of step width  $\bar{W}$  on the apparent contact angle for a step height of  $\bar{H} = 0.64 \pm 0.05$  and groove widths of (a)  $\bar{G} = 0.16 \pm 0.01$  and (b)  $\bar{G} = 0.64 \pm 0.05$ . The solid lines represent predictions of the mathematical model in ref 29, and the symbols correspond to MD simulations. The vertical error bar depicts the representative uncertainty in the MD contact angles, and the horizontal error bars indicate the uncertainty in the MD value of  $R_0$ .

droplet sizes, for which the effect of gravity is negligible. This indicates that nanoscale MD simulation can reproduce many experimentally observed features of droplet wetting on patterned surfaces for the same feature-to-droplet size ratio and in the small Bond number limit, provided that the droplet in the MD simulation is sufficiently large for its interfacial energies to exhibit continuum-like behavior.

Going beyond this agreement, we demonstrate how MD simulations can indicate wetting-mode multiplicity due to the existence of free-energy barriers between various droplet configurations. Wetting-mode multiplicity is observed experimentally,<sup>13–22</sup> and it is difficult to capture this effect accurately with analytical models. To show how the final observed configuration of a droplet is influenced by its initial configuration, we considered the same droplet in three different initial configurations, as shown in the top panels of Figures 8 and 9. In the first of these, which can be seen in Figures 8A(i), C(i) and 9A(i), the drop is initially in the Cassie mode with its center of mass over a groove. In the second initial configuration, the drop is in the Wenzel mode, as shown in Figures 8B(i), D(i) and 9B(i). Finally, for the third initial condition, the droplet is in the Cassie mode with its center of mass over a step, as shown in Figure 9C(i). The final configuration of the droplet after 10 ns of MD simulation starting with each of these initial states is shown in Figures 8A(f)–D(f) and 9A(f)–C(f).

We find that wetting-mode multiplicity is strongly dependent on the topography of the surface. For narrow steps ( $\bar{W} = 0.32$

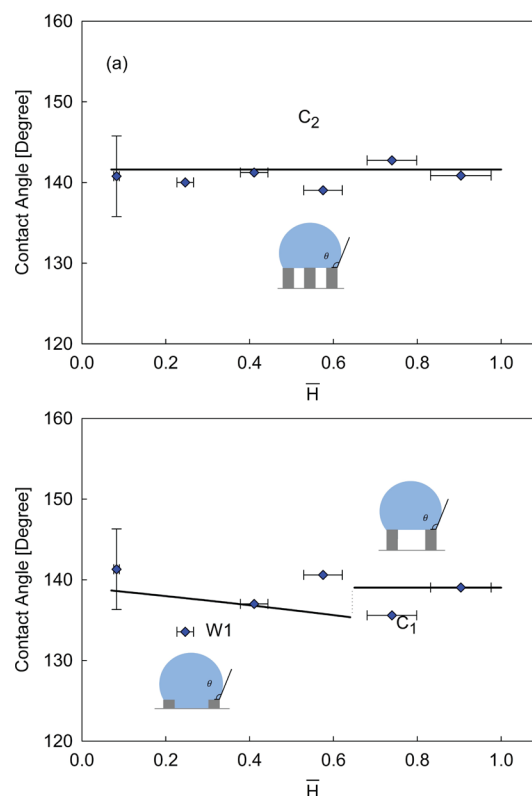


**Figure 7.** Effect of step height  $\bar{H}$  on the apparent contact angle for a step width of  $\bar{W} = 0.32 \pm 0.03$  and groove widths (a)  $\bar{G} = 0.16 \pm 0.01$  and (b)  $\bar{G} = 0.45 \pm 0.04$ . The solid lines represent predictions of the mathematical model in ref 29, and the symbols correspond to MD simulations. The vertical error bar depicts the representative uncertainty in the MD contact angles, and the horizontal error bars indicate the uncertainty in the MD value of  $R_0$ .

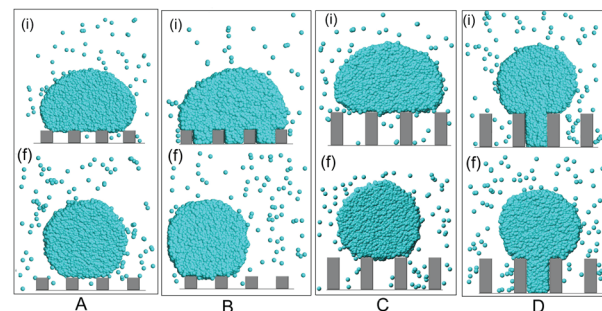


**Figure 8.** Effect of initial droplet configuration (i) on the final wetting configuration (f) realized in MD simulation for surfaces with  $\bar{W} = 0.32 \pm 0.03$  and  $\bar{H} = 0.32 \pm 0.03$ ,  $\bar{G} = 0.40 \pm 0.03$  (A and B), and  $\bar{H} = 0.8 \pm 0.06$ ,  $\bar{G} = 0.48 \pm 0.04$  (C and D).

$\pm 0.03$ ), the observed wetting mode is unique and independent of the initial configuration of the droplet when  $\bar{H} = 0.40 \pm 0.03$  and  $\bar{G} = 0.48 \pm 0.04$ . An example of this wetting-mode uniqueness is shown in panels A and B in Figure 8, where the droplet's final configuration is  $C_1$  regardless of whether it is initially in a Cassie or Wenzel configuration. However, as the groove width increases to  $\bar{G} = 0.48 \pm 0.04$  and the step height increases to  $\bar{H} = 0.40 \pm 0.03$ , wetting-mode multiplicity appears, as shown by panels C and D in Figure 8. Here, when the droplet is initially in the Cassie mode (Figure 8C(i)), its final configuration is  $C_1$  (Figure 8C(f)), whereas the Wenzel

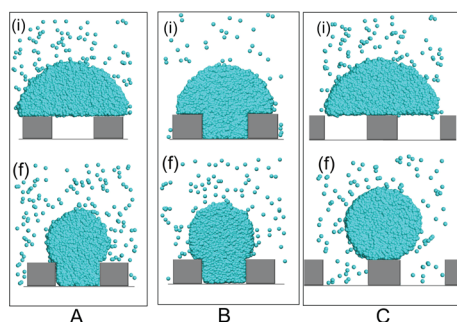


**Figure 9.** Effect of initial droplet location (i) on the final observed wetting configuration (f) for surfaces with a pattern comparable to the drop size. (A–C)  $\bar{H} = 0.64 \pm 0.05$ ,  $\bar{G} = 1.12 \pm 0.09$ , and  $\bar{W} = 0.8 \pm 0.06$ .

initial configuration (Figure 8D(i)) leads to a  $W_1$  final configuration (Figure 8D(f)).

Figure 9 shows an example in which both the Wenzel and epitaxial Cassie states are observed for the same surface topography with different initial conditions. When the initial configuration of the droplet is either a Cassie state, with the center of mass over a groove, or a Wenzel state (panels A and B in Figure 9), the final configuration of the drop is the  $W_1$  mode. For a Cassie initial configuration with the center of mass over a step, the drop achieves an epitaxial Cassie final configuration (Figure 9 C(f)). When the final wetting state depends on the initial position of the droplet, there is a free-energy barrier separating the metastable state(s) from the global-minimum free-energy state. On the basis of the results here, we cannot comment on the magnitude of the free-energy barrier for a given transition in a macroscopic system. Theoretical methods exist to quantify these barriers within MD simulations,<sup>51–53</sup> and this would be an interesting problem for future studies. However, without applying these special techniques, canonical MD simulations can indicate the morphological trends that are likely to lead to wetting-state multiplicity in a macroscopic system.

We can combine our observations of the wetting modes and contact angles to construct a phase diagram of possible wetting modes as a function of the scaled geometrical parameters describing the surface. Our computational results lead to a 3D phase diagram in terms of  $\bar{H}$ ,  $\bar{G}$ , and  $\bar{W}$ , covering parameter ranges of  $[0.08, 1.2]$ ,  $[0.08, 0.8]$ , and  $[0.16, 0.8]$ , respectively. The increment sizes for  $\bar{H}$ ,  $\bar{G}$ , and  $\bar{W}$  used in the search were 0.08, 0.04, and 0.16, respectively. For each set of surface parameters, we considered three different initial droplet configurations (Cassie with the droplet center of mass over a groove, Cassie with the center of mass over a step, and Wenzel). Two different constant- $\bar{W}$  cross sections of the wetting phase diagram on a hydrophobic surface with  $\theta_e = 126 \pm 5^\circ$  are shown in Figures 10 and 11. To construct these cross sections, we considered fixed values of  $\bar{H}$  and  $\bar{W}$  with a given initial condition, and we searched for the critical value of  $\bar{G}$  at which a wetting-mode transition occurred. To compare the MD phase diagrams to those obtained from the macroscopic model, phase boundaries between the most stable wetting modes predicted by the macroscopic model are shown by dashed lines in Figures 10 and 11. Regions I–III correspond to model predictions for the Wenzel, Cassie, and epitaxial Cassie wetting modes, respectively.

Figures 10 and 11 show that the Cassie state becomes favorable for narrow grooves and tall steps. Conversely, the

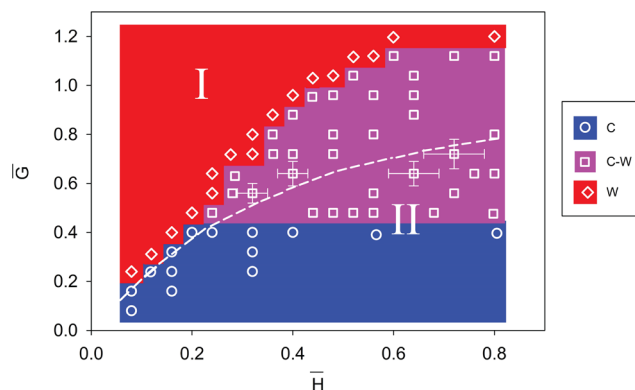


**Figure 10.** Cross-section of the wetting phase diagram for a hydrophobic surface with  $\theta_e = 126^\circ$  and  $\bar{W} = 0.16 \pm 0.01$ . Data points from the simulations are represented by symbols, and colored regions indicate the predicted wetting regimes based on the simulations. Error bars have been shown for only a few points to improve visual clarity. However, the uncertainty in both  $\bar{H}$  and  $\bar{G}$  ranged from 0.01 to 0.09. Phase boundaries between the most stable wetting modes predicted by the macroscopic model<sup>29</sup> are shown by dashed lines, and regions I and II correspond to the model predictions for Wenzel and Cassie modes, respectively.

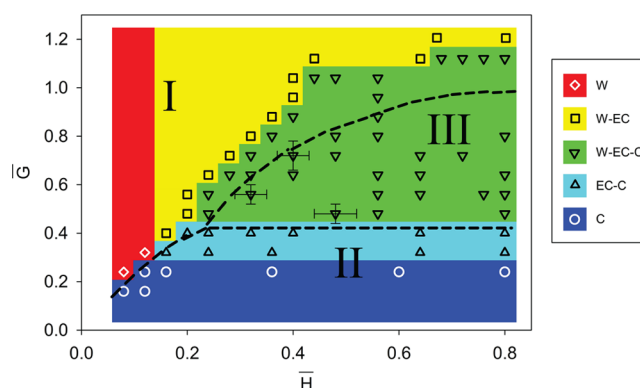


**Figure 11.** Cross-section of the wetting phase diagram for a hydrophobic surface with  $\theta_e = 126^\circ$  and  $\bar{W} = 0.8 \pm 0.06$ . Data points from the simulations are represented by symbols, and colored regions indicate the predicted wetting regimes based on the simulations. Error bars have been shown for only a few points to improve visual clarity. However, the uncertainty in both  $\bar{H}$  and  $\bar{G}$  ranged from 0.01 to 0.09. Phase boundaries between the most stable wetting modes predicted by the mathematical model<sup>31</sup> are shown by dashed lines, and regions I–III correspond to the model predictions for Wenzel, Cassie, and epitaxial Cassie domains, respectively.

Wenzel state is observed for wide grooves and short steps. The epitaxial Cassie (EC) mode appears when the dimensions of the surface pattern become comparable to the size of the droplet (i.e., for wide and tall steps separated by sufficiently wide grooves). These figures also show that the most stable wetting mode predicted by the macroscopic model is always among the wetting modes observed in MD simulations. However, MD simulations exhibit wetting-mode multiplicity in the regions neighboring wetting-mode boundaries predicted by the model. For the narrow steps ( $\bar{W} = 0.16 \pm 0.01$ ) in Figure 10, only two wetting-mode domains (Cassie and Wenzel) with a single two-phase boundary are predicted by the model. The MD simulations also result in a dual-mode (Cassie–Wenzel) region in the vicinity of the predicted Cassie–Wenzel boundary. For the wider ( $\bar{W} = 0.80 \pm 0.06$ )



steps in Figure 11, a more complex wetting behavior is observed in MD simulations, with both dual-mode and triple-mode regions being realized. This is due to the presence of a third wetting mode (i.e., epitaxial Cassie) for wide steps. In this case, the macroscopic model predicts three two-phase boundaries that meet at the triple point  $(\bar{G}, \bar{H}) = (0.44 \pm 0.03, 0.23 \pm 0.02)$  in Figure 11. The triple mode (epitaxial Cassie–Wenzel–Cassie) region resulting from MD simulations is quite large, encompassing nearly the entire model-predicted epitaxial Cassie domain for  $\bar{H} < 0.80$  and indicating the presence of (presumably) metastable Cassie states within the model-predicted Wenzel region around the Wenzel–epitaxial Cassie boundary. This is likely due to a large free-energy barrier for the transition from the Cassie to the epitaxial Cassie state when the groove width is comparable to the drop size. Nevertheless, there is good agreement between the model and MD simulation results in all three regions in the sense that the most stable mode predicted by the model is always among the modes realized by MD simulations.

## CONCLUSIONS

We investigated the wetting behavior of an LJ cylindrical droplet on a periodically grooved surface by using MD simulations. A systematic study on the effect of surface topographical parameters revealed that the drop size is an appropriate length scale for characterizing wetting states and their corresponding contact angles, implying that nanoscale MD simulations can be used to predict macroscale wetting behavior. This observation is consistent with our previously derived<sup>29</sup> thermodynamic model for droplet wetting in the limit of a negligible effect of gravity. Good agreement was found between contact angles obtained in MD simulations and those predicted by our macroscopic model.<sup>29</sup> We constructed drop-size-independent wetting phase diagrams representing possible wetting configurations of a droplet as a function of surface topography. Here, we found that the most stable wetting mode predicted by the macroscopic model is always among the wetting modes observed in MD simulations. However, a droplet can achieve multiple wetting modes for a given surface morphology, with each corresponding to a stable or metastable state. Metastability is especially prevalent near wetting-mode boundaries. The drop can remain trapped in metastable states over relatively long time scales as a result of the presence of free-energy barriers impeding wetting-mode transitions. A similar phenomenon has been observed experimentally. Thus, our studies indicate that suitably applied MD simulations can yield insight into the large-length-scale behavior of droplets on patterned surfaces. Such simulations can play a role in the design of patterned surfaces for optimal wettability.

## AUTHOR INFORMATION

### Corresponding Author

\*E-mail: fichthorn@psu.edu.

### Notes

The authors declare no competing financial interest.

## ACKNOWLEDGMENTS

This work was supported by grant CBET 0730987 from the National Science Foundation. We acknowledge assistance from Mr. Jin Pyo Hong.

## REFERENCES

- (1) Li, X.; Reinhoudt, M.; Crego-Calama, M. What do we need for a superhydrophobic surface? A review on the recent progress in the preparation of superhydrophobic surfaces. *Chem. Soc. Rev.* **2007**, *36*, 1350–1368.
- (2) Roach, P.; Shirtcliffe, N. J.; Newton, M. I. Progress in superhydrophobic surface development. *Soft Matter* **2008**, *4*, 224–240.
- (3) Yan, Y. Y.; Gao, N.; Barthlott, W. Mimicking natural superhydrophobic surfaces and grasping the wetting process: A review on recent progress in preparing superhydrophobic surfaces. *Adv. Colloid Interface Sci.* **2001**, *169*, 80–105.
- (4) Bhushan, B.; Jung, Y. C. Natural and biomimetic artificial surfaces for superhydrophobicity, self-cleaning, low adhesion, and drag reduction. *Prog. Mater. Sci.* **2011**, *56*, 1–108.
- (5) Bormashenko, E.; Gendelman, O.; Whyman, G. Superhydrophobicity of lotus leaves versus birds wings: different physical mechanisms leading to similar phenomena. *Langmuir* **2012**, *28*, 14992–14997.
- (6) Wenzel, R. N. Resistance of solid surfaces to wetting by water. *Ind. Eng. Chem.* **1936**, *28*, 988–994.
- (7) Cassie, A. B. D.; Baxter, S. Wettability of porous surfaces. *Trans. Faraday Soc.* **1944**, *40*, 546–551.
- (8) Gao, L.; McCarthy, T. J. How Wenzel and Cassie were wrong. *Langmuir* **2007**, *23*, 3762–3765; *Langmuir* **2007**, *23*, 3762–3765.
- (9) Marmur, A.; Bittoun, E. When Wenzel and Cassie are right: reconciling local and global considerations. *Langmuir* **2009**, *25*, 1277–1281.
- (10) McHale, G. Cassie and Wenzel: were they really so wrong? *Langmuir* **2007**, *23*, 8200–8205.
- (11) Erbil, H. Y.; Cansoy, C. E. Range of applicability of the Wenzel and Cassie–Baxter equations for superhydrophobic surfaces. *Langmuir* **2009**, *25*, 14135–14145.
- (12) Cansoy, C. E.; Erbil, H. Y.; Akar, O.; Akin, T. Effect of pattern size and geometry on the use of Cassie–Baxter equation for superhydrophobic surfaces. *Colloids Surf., A* **2011**, *386*, 116–124.
- (13) He, B.; Patankar, N. A.; Lee, J. Multiple equilibrium droplet shapes and design criterion for rough hydrophobic surfaces. *Langmuir* **2003**, *19*, 4999–5003.
- (14) Patankar, N. A. Transition between superhydrophobic states on rough surfaces. *Langmuir* **2004**, *20*, 7097–7102.
- (15) Barbieri, L.; Wagner, E.; Hoffmann, P. Water wetting transition parameters of perfluorinated substrates with periodically distributed flat-top microscale obstacles. *Langmuir* **2007**, *23*, 1723–1734.
- (16) DeConinck, J.; Dunlop, F.; Huillet, T. Metastable wetting. *J. Stat. Mech.* **2011**, P06013.
- (17) Liu, G.; Fu, L.; Rode, A. V.; Craig, V. S. J. Water droplet motion control on superhydrophobic surfaces: exploiting the Wenzel-to-Cassie transition. *Langmuir* **2011**, *27*, 2925–2600.
- (18) Ran, C.; Ding, G.; Liu, W.; Deng, Y.; Hou, W. Wetting on nanoporous alumina surface: transition between Wenzel and Cassie states controlled by surface structure. *Langmuir* **2008**, *24*, 9952–9955.
- (19) Lafuma, A.; Quere, D. Superhydrophobic states. *Nat. Mater.* **2003**, *2*, 457–460.
- (20) Bahadur, V.; Garimella, S. V. Preventing the Cassie–Wenzel transition using surfaces with noncommunicating roughness elements. *Langmuir* **2009**, *28*, 48115–4820.
- (21) Bormashenko, E.; Pogreb, R.; Whyman, G.; Erlich, M. Resonance Cassie–Wenzel wetting transition for horizontally vibrated drops deposited on a rough surface. *Nat. Mater.* **2007**, *23*, 12217–12221.
- (22) Nosonovsky, M.; Bhushan, B. Biomimetic superhydrophobic surfaces: multiscale approach. *Nano Lett.* **2007**, *9*, 2633–2637.
- (23) Daub, C. D.; Wang, J.; Kudesia, S.; Bratko, D.; Luzar, A. The influence of molecular-scale roughness on the surface spreading of an aqueous nanodrop. *Faraday Discuss.* **2010**, *146*, 67–77.
- (24) Yong, X.; Zhang, L. T. Nanoscale wetting on groove-patterned surfaces. *Langmuir* **2009**, *25*, 5045–5053.

- (25) Wu, H.; Borhan, A.; Fichthorn, K. A. Coarse-grained interaction of a fluid with a physically-patterned solid surface: application to nanodroplet wetting. *J. Low Temp. Phys.* **2009**, *157*, 277–295.
- (26) Hirvi, J. T.; Pakkanen, T. A. Nanodroplet impact and sliding on structured polymer surfaces. *Surf. Sci.* **2008**, *602*, 1810–1818.
- (27) Lundgren, M.; Allan, N. L.; Cosgrove, T. Modeling of wetting: a study of nanowetting at rough and heterogeneous surfaces. *Langmuir* **2007**, *23*, 1187–1194.
- (28) Hirvi, J. T.; Pakkanen, T. A. Enhanced hydrophobicity of rough polymer surfaces. *J. Phys. Chem. B* **2007**, *111*, 3336–3341.
- (29) Shahraz, A.; Borhan, A.; Fichthorn, K. A. A theory for the morphological dependence of wetting on a physically-patterned solid surface. *Langmuir* **2012**, *28*, 14227–1423.
- (30) Leroy, F.; Mueller-Plathe, F. Can continuum thermodynamics characterize Wenzel wetting states of water at the nanometer scale? *J. Chem. Theory Comput.* **2012**, *8*, 3724–3732.
- (31) Koishi, T.; Yasuoka, K.; Fujikawa, S.; Ebisuzaki, T.; Zeng, X. C. Coexistence and transition between Cassie and Wenzel state on pillared hydrophobic surface. *Proc. Natl. Acad. Sci. U.S.A.* **2009**, *106*, 8435–8440.
- (32) Savoy, E. S.; Escobedo, F. A. Molecular simulations of wetting of a rough surface by an oily fluid: effect of topology, chemistry, and droplet size on wetting transition rates. *Langmuir* **2012**, *28*, 3412–3419.
- (33) Savoy, E. S.; Escobedo, F. A. Simulation study of free-energy barriers in the wetting transition of an oily fluid on a rough surface with reentrant geometry. *Langmuir* **2012**, *28*, 16080–16090.
- (34) Giacomello, A.; Meloni, S.; Chinappi, M.; Casciola, C. M. Cassie-Baxter and Wenzel states on a nanostructured surface: phase diagram, metastabilities, and transition mechanism by atomistic free energy calculations. *Langmuir* **2012**, *28*, 10764–10772.
- (35) Giacomello, A.; Chinappi, M.; Meloni, S.; Casciola, C. M. Metastable wetting on superhydrophobic surfaces: Continuum and atomistic views of the Cassie-Baxter–Wenzel transition. *Phys. Rev. Lett.* **2012**, *109*, 226102.
- (36) Koishi, T.; Yasuoka, K.; Fujikawa, S.; Zeng, X. C. Measurement of contact-angle hysteresis for droplets on nanopillared surface and in the Cassie and Wenzel states: a molecular dynamics simulation study. *ACS Nano* **2011**, *5*, 6834–6842.
- (37) Malani, A.; Raghavanpillai, A.; Wysong, E. B.; Rutledge, G. C. Can dynamic contact angle be measured using molecular modeling? *Phys. Rev. Lett.* **2012**, *109*, 184501.
- (38) Wang, F.-C.; Zhao, U.-P. Contact angle hysteresis at the nanoscale: a molecular dynamics simulation study. *Colloid Polym. Sci.* **2013**, *291*, 307–315.
- (39) Weijs, J. H.; Snoeijer, J. H.; Lohse, D. Formation of surface nanobubbles and the universality of their contact angles: a molecular dynamics approach. *Phys. Rev. Lett.* **2012**, *108*, 104501.
- (40) Ritos, K.; Dongari, N.; Borg, M. K.; Zhang, Y.; Reese, J. M. Dynamics of nanoscale droplets on moving surfaces. *Langmuir* **2013**, *29*, 6936–6943.
- (41) Heine, D. R.; Grest, G. S.; Webb, E. B. Spreading dynamics of polymer nanodroplets in cylindrical geometries. *Phys. Rev. E* **2004**, *70*, 011606.
- (42) Weijs, J. H.; Marchand, A.; Andreotti, B.; Lohse, D.; Snoeijer, J. H. Origin of line tension for a Lennard-Jones nanodroplet. *Phys. Fluids* **2011**, *23*, 022001.
- (43) Nosé, S. Constant temperature molecular dynamics methods. *Prog. Theor. Phys. Suppl.* **1991**, *103*, 1–46.
- (44) Hoover, W. G. Canonical dynamics: equilibrium phase-space distributions. *Phys. Rev. A* **1985**, *31*, 1695–1697.
- (45) Wu, H.; Borhan, A.; Fichthorn, K. A. Interaction of fluids with physically patterned solid surfaces. *J. Chem. Phys.* **2010**, *133*, 054704.
- (46) Wolf, F. G.; dos Santos, L. O. E.; Philippi, P. C. Modeling and simulation of the fluid-solid interaction in wetting. *J. Stat. Mech. Theor. Exp.* **2009**, P06008.
- (47) Extrand, C. W. Modeling of ultralyophobicity: suspension of liquid drops by a single asperity. *Langmuir* **2005**, *21*, 10370–10374.
- (48) Tóth, T.; Ferraro, D.; Chiarello, E.; Pierno, M.; Mistura, G.; Bissacco, G.; Sempredon, C. Suspension of water droplets on individual pillars. *Langmuir* **2011**, *27*, 4742–4748.
- (49) Öner, D.; McCarthy, T. J. Ultrahydrophobic surfaces. Effects of topography length scales on wettability. *Langmuir* **2000**, *16*, 7777–7782.
- (50) Yang, J.; Rose, F. R. A. J.; Gadegaard, N.; Alexander, M. R. Effect of sessile drop volume on the wetting anisotropy observed on grooved surfaces. *Langmuir* **2009**, *25*, 2567–2571.
- (51) Bonella, S.; Meloni, S.; Ciccotti, G. Theory and methods for rare events. *Eur. Phys. J. B* **2012**, *85*, 97.
- (52) R. J. Allen, R. J.; Valeriani, C.; ten Wolde, P. R. Forward flux sampling for rare event simulations. *J. Phys.: Condens. Matter* **2009**, *21*, 463102.
- (53) Borrero, E. E.; Escobedo, F. A. Reaction coordinates and transition pathways of rare events via forward flux sampling. *J. Chem. Phys.* **2007**, *127*, 164101.